[COR: alpha]

A family of memristive multibutterfly chaotic systems with multidirectional initial-based offset boosting

Hairong Lin[a], Chunhua Wang[a,*], Sichun Du[a], Wei Yao[b] and Yichuang Sun[c]

[a]College of Computer Science and Electronic Engineering, Hunan University, Changsha 410082, China
[b]School of Computer and Communication Engineering, Changsha University of Science and Technology, Changsha 410114, China.
[c]School of Engineering and Computer Science, University of Hertfordshire, Hatfield AL10 9AB, U.K

ARTICLE INFO

Keywords:
Memristive chaotic system
multibutterfly attractor
initial-offset behavior
chaotic circuit design
medical image encryption

ABSTRACT

Memristors are commonly used to construct memristive chaotic systems with complex dynamics because of their strong nonlinearity and unique memory effects. In this paper, a simplified multi-piecewise memristor is applied for designing a family of memristive multibutterfly chaotic systems (MMBCSs). By coupling different numbers of the simplified multi-piecewise memristors into a modified Sprott C system, three MMBCSs are constructed. Theoretical analysis and numerical simulations show that the three MMBCSs can not only generate connected 1D(direction)-, 2D(plane)-, and 3D(space)-multibutterfly chaotic attractors (MBCAs), respectively, but also can respectively produce unconnected 1D-, 2D-, and 3D-MBCAs. Also, the number and position of butterfly attractors can be easily controlled by switching the memristor's integer parameters and initial states, respectively. More importantly, the constructed three MMBCSs exhibit different initial-based offset boosting including 1D-, 2D-, and 3D-boosting behaviors, respectively. Especially, the 3D-initial-offset behavior is found in chaotic systems at the first time. Furthermore, we further implement the physical circuit of the three MMBCSs, and various typical dynamical behaviors are demonstrated by hardware experiments and Multisim simulations. Finally, a medical image encryption solution for online medical treatment is designed based on the proposed MMBCSs.

1. Introduction

Chaotic systems have attracted great attention from academic and industrial fields due to their potential applications in information security [1–3]. Since the Lorenz chaotic system was proposed in 1963 [4], more than thousands of chaotic systems have been constructed to generate complex dynamical behaviors [5–7]. In recent years, the construction of memristive chaotic systems has become a hot research topic. Due to special nonlinearity and memory characteristics of memristor, the memristive chaotic systems exhibit complex dynamical phenomena such as coexisting attractors [8–10], multistability [11, 12], extreme multistability [13, 14], Initial-offset behaviors [15, 16], and so on [17, 18]. Thanks to these significant characteristics, the memristive chaotic systems are studied and widely applied in designing pseudorandom number generators (PRNG) [19] or chaos-based cryptosystems [20].

Over the past decades, many scholars have done much deep and extensive research on the design of chaotic systems. Among them, one important work is to design multiscroll/wing chaotic systems [21–24]. Compared with single-scroll/wing chaotic systems, the multiscroll/wing chaotic systems have higher randomness and tunability and have a wider application range [25, 26]. A chaotic system with multiple butterfly attractors is called a multibutterfly chaotic system (MBCS) [27, 28] which integrates the attractor features of multiwing chaotic systems and multiscroll chaotic systems. Because of its multiwing and multiscroll characteristics, the MBCS has attracted great interest from chaos researchers [29–31]. In recent years, various MBCSs with different characteristics have been proposed. For example, to further enhance chaos, Yu *et al.* [32] proposed hyperchaotic 1D- and 2D-MBCSs by constructing switch controllers and super-heteroclinic loops in a Lorenz-like chaotic system. By using a nonlinear piecewise-line function, Wang *et al.* [33] designed a hidden hyperchaotic 1D-MBCS. Yu *et al.* [34] constructed a 2D-MBCS by applying rotation transformation to a Lorenz-like system. To simplify the circuit implementation, Hong *et al.* [35] proposed 1D-, 2D-,

*Corresponding author
wch1227164@hnu.edu.cn (C. Wang)
ORCID(s):

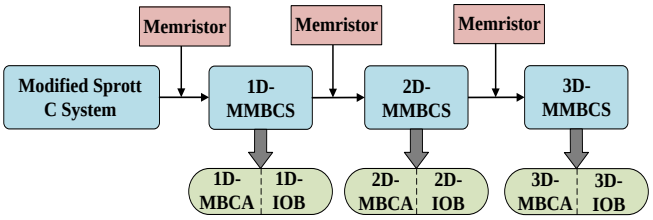

Figure 1: Design flow of MMBCSs.

and 3D-MBCSs by adopting a multilevel-logic pulse control method. Lin *et al.* [36] proposed an extremely simple 1D-MBCS based on a modified Sprott-like chaotic system.

The memristor first fabricated by HP lab in 2008 [37] is a nonlinear circuit element. Due to excellent nonlinear and memory effect [38], the memristor is often applied to existing chaotic circuits and systems to generate more complex dynamical behaviors [39–41]. Two memristors are added to Chua's circuit by Chen *et al.* [42] to generate a five-dimensional Chua's circuit with extreme multistability. Jiang *et al.* [43] constructed a hyperchaotic Jerk system with complete amplitude control by introducing two memristors into a Jerk chaotic system. By coupling a discrete memristor into the Logistic map, Bao *et al.* [44] presented a memristive Logistic map with hyperchaos. Recently, the memristor has been explored to construct memristive multiscroll/wing chaotic systems. For instance, by adding a memristor to an existing multiwing chaotic system, Zhou *et al.* [45] proposed a memristive multiwing chaotic system with hidden hyperchaos. Zhang *et al.* [46] constructed a multistable memristive multiscroll chaotic system by coupling one memristor into Chua's system. Additionally, adopting the same approach to the Sprott A system, a hidden memristive 1D-multibutterfly chaotic system with multistability is proposed by Zhang *et al.* [47]. According to the literature review above, the memristor has great application prospects in the design of multiwing chaotic systems. However, so far, a multibutterfly chaotic system with multidirectional initial-offset coexisting behaviors has not been reported. Due to the characteristics of both multibutterfly chaotic attractors and multidirectional initial-offset coexisting behaviors, such chaotic systems have a greater prospect in chaos-based engineering applications. In this work, different numbers of memristors are introduced into a modified Sprott C system to construct three different memristive multibutterfly chaotic systems including 1D-, 2D-, and 3D-MMBCSs. It is found that the constructed three MMBCSs not only can respectively generate connected and unconnected 1D-, 2D-, and 3D-MBCAs, but also can respectively exhibit 1D-, 2D-, and 3D-initial-offset behavior (3D-IOB). The MMBCSs are designed as shown in Fig.1.

The main contributions of this work include the following four points:

1) Different from the memristive multiscroll/wing chaotic systems proposed in [45–47], a family of MMBCSs is respectively constructed based on the modified Sprott C system by coupling different numbers of memristors to different dimensions.

2) Unlike the MBCSs reported in [27–36], the proposed MMBCSs can not only generate 1D-, 2D-, and 3D-connected and unconnected multibutterfly chaotic attractors, respectively, but also respectively show 1D-, 2D-, and 3D-initial-based offset boostings.

3) Arbitrary number and position of connected and unconnected multibutterfly chaotic attractors can be obtained by adjusting memristors' integer parameters and switching memristors' initial states, respectively, which can meet the signal requirement in industrial applications.

4) A medical image encryption solution based on the proposed MMBCSs is designed and applied in online medical treatment.

The rest of this paper is arranged as follows. In Section 2, we propose three MMBCSs. The dynamical characteristics of the three MMBCSs are orderly analyzed in Section 3. In Section 4, comparison analysis and circuit verification are presented. A medical image encryption solution based on the MMBCSs are designed in Section 5. Finally, Section 6 concludes this paper.

2. Design of memristive multibutterfly chaotic systems

This section first proposes a simplified multi-piecewise nonlinear memristor model, then designs three memristive multibutterfly chaotic systems by introducing the different number of memristors into a modified Sprott C system.

2.1 Brief introduction of the memristor model

Memristors with nonlinearity and memory are often introduced into existing chaotic systems to enhance chaos complexity. Recently, Zhang *et al.* [46] designed an interesting multi-piecewise nonlinear memristor to generate multiscroll chaotic attractors, and its mathematical model can be expressed as

$$\begin{cases} i = W(\varphi)v = (a + bh(\varphi))v \\ \mathrm{d}\varphi/\mathrm{d}t = cv - dh(\varphi) \end{cases} \tag{1}$$

where $h(\varphi)$ is divided into two parts, namely, $h_N(\varphi)$ and $h_M(\varphi)$:

$$h_N(\varphi) = \begin{cases} \varphi, N = 0 \\ \varphi - \sum_{i=1}^{N} (\mathrm{sgn}(\varphi + (2i-1)) + \mathrm{sgn}(\varphi - (2i-1))), \\ N = 1, 2, 3, \ldots \end{cases} \tag{2}$$

$$h_M(\varphi) = \begin{cases} \varphi - \mathrm{sgn}(\varphi), M = 0 \\ \varphi - \mathrm{sgn}(\varphi) - \sum_{j=1}^{M} (\mathrm{sgn}(\varphi + 2j) + \mathrm{sgn}(\varphi - 2j)), \\ M = 1, 2, 3, \ldots \end{cases} \tag{3}$$

where N and M are two adjustable integer parameters, $h_N(\varphi)$ and $h_M(\varphi)$ are used to generate odd-numbered multiscrolls and even-numbered multiscrolls, respectively. Compared with other memristor models [8, 9, 11–14], this memristor has much higher adjustability and diversity due to its controllable parameters N and M. This property is important for the generation of multi-attractors. Inspired by the memristor model, a simplified multi-piecewise nonlinear memristor model is proposed as follows

$$\begin{cases} i = W(\varphi)v = b\varphi v \\ \mathrm{d}\varphi/\mathrm{d}t = cv - dh(\varphi) \end{cases} \tag{4}$$

The mathematical model of the proposed memristor in (4) is greatly simplified because its memductance $W(\varphi)$ has no polynomial functions $h(\varphi)$. Meanwhile, compared with the original memristor circuit in [46], its equivalent circuit is also simplified as shown in Fig.2.

Taking M=2 as an example, the numerical simulation results in Matlab and circuit simulation results in Multisim are given in Fig.3(a) and Fig.3(b), respectively. From Fig.3(a), when b=0.1, c=d=2, M=2, $v = A\sin(2\pi Ft)$ (A=4, F=2, 4, 16), the memristor model in (4) exhibits three memristive features [38]. Correspondingly, in Fig.2, when closing control switches S_1, S_2, and S_3, setting e_1=2 V, e_2=4 V, R_b=gR/b=10 kΩ, R_c=R_d=R/c=5 kΩ, C=1 nF, $V = H\sin(2\pi ft)$ (H=4 V, f=20, 40, 160 MHz), the memristor circuit generates the corresponding pinched hysteresis loops, as shown in Fig.3(b). It should be pointed out that by choosing different control voltages (e_i) and switches (S_i), the memristors with different values of N and M can be implemented. For example, when closing switches S_1, S_2, and S_3, setting control voltages e_1=2 V and e_2=4 V, the memristor with M=2 can be realized. On the contrary, when only closing switches S_2 and S_3, setting control voltages e_1=1 V and e_2=3 V, the memristor with N=2 can be realized.

2.2 Models of memristive multibutterfly chaotic systems

The Sprott C system has been widely studied because of its butterfly chaotic attractors [48]. However, they also have some drawbacks of small initial range, poor ergodicity, and weak chaos. A modified Sprott C can be described by

$$\begin{cases} \dot{x} = \alpha(z - x) \\ \dot{y} = \beta - z^2 \\ \dot{z} = \gamma xy \end{cases} \tag{5}$$

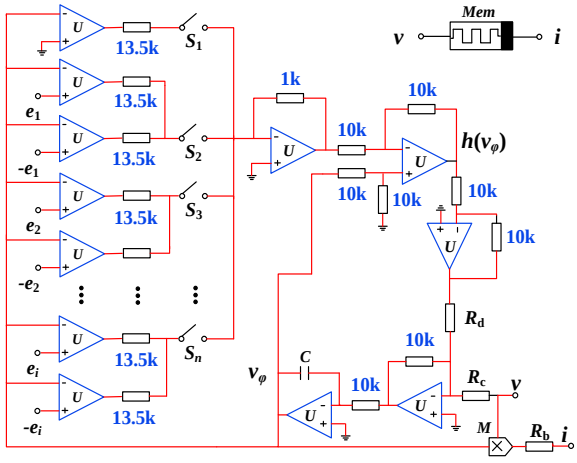

Figure 2: Simplified multi-piecewise memristor circuit.

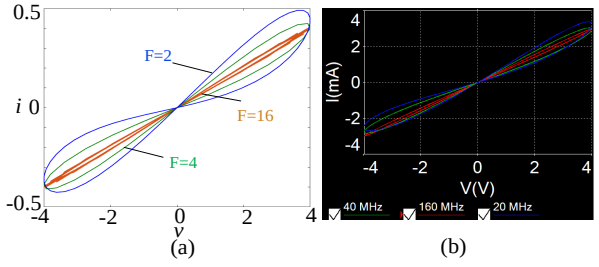

Figure 3: Hysteresis loop features of the simplified multi-piecewise memristor. (a) Numerical simulation. (b) Circuit simulation.

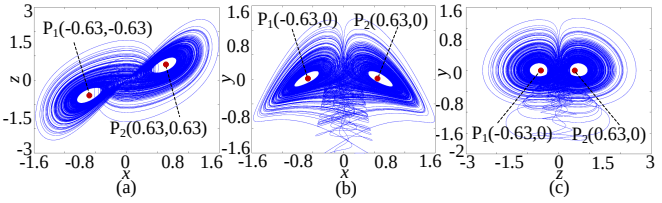

Figure 4: Butterfly chaotic attractor of the system (4). (a) x-z plane. (b) x-y plane. (b) z-y plane.

with α=2, β=0.4, and γ=8, and initial states (0.1, 0.1, 0.1), system (5) can generate a classical butterfly chaotic attractor with two nonhyperbolic equilibrium points (P_1 and P_2) with a pair of pure imaginary eigenvalues, as shown in Fig.4.

To further enhance the chaos complexity and enrich the dynamical behavior of the modified Sprott C system, the proposed multi-piecewise memristor in (4) is coupled into the system (5) to construct memristive multibutterfly chaotic systems. From Fig.1, by coupling different number of memristors into the modified Sprott C system, three MMBCSs can be constructed. For example, coupling one memristor, a 1D-MMBCS can be described as

$$\begin{cases} \dot{x} = \alpha(z - x) + k_1 x W(\varphi) \\ \dot{y} = \beta - z^2 \\ \dot{z} = \gamma x y \\ \dot{\varphi} = c_1 x - d_1 h(\varphi) \end{cases} \tag{6}$$

Coupling two memristors, a 2D-MMBCS can be described as

$$\begin{cases} \dot{x} = \alpha(z - x) + k_1 x W(\varphi_1) \\ \dot{y} = \beta - z^2 + k_2 y W(\varphi_2) \\ \dot{z} = \gamma x y \\ \dot{\varphi}_1 = c_1 x - d_1 h_1(\varphi_1) \\ \dot{\varphi}_2 = c_2 y - d_2 h_2(\varphi_2) \end{cases} \tag{7}$$

Coupling three memristors, a 3D-MMBCS can be described as

$$\begin{cases} \dot{x} = \alpha(z - x) + k_1 x W(\varphi_1) \\ \dot{y} = \beta - z^2 + k_2 y W(\varphi_2) \\ \dot{z} = \gamma x y + k_3 z W(\varphi_3) \\ \dot{\varphi}_1 = c_1 x - d_1 h_1(\varphi_1) \\ \dot{\varphi}_2 = c_2 y - d_2 h_2(\varphi_2) \\ \dot{\varphi}_3 = c_3 z - d_3 h_3(\varphi_3) \end{cases} \tag{8}$$

In the above systems, k_1, k_2, and k_3 are coupling coefficients, c_1, c_2, c_3, d_1, d_2, and d_3 are memristive parameters, and N_i/M_i $(i = 1, 2, 3)$ are the control parameters of the i-th memristor, respectively. Noted that only one of the parameters ($N_i and M_i$) can be used at the same time.

3. Analysis of dynamical characteristics

In this section, various special dynamical behaviors in the three MMBCSs are revealed by using various nonlinear dynamics analysis methods including equilibrium point distribution and stability, phase portraits, basin of attraction, bifurcation diagrams, and Lyapunov exponents. Noted that the ODE45 algorithm is utilized in the Matlab numerical simulation, where the start time, the time step, and the time length are fixed as 500, 0.01, and 5000, respectively.

3.1 Dynamical analysis of 1D-MMBCS

This subsection analyzes the equilibrium points, 1D-MBCAs, and 1D-Initial-offset behavior of the 1D-MMBCS in the system (6). Equilibrium points and their stabilities are commonly used to find various chaotic phenomena and reveal their generation mechanism in dynamical systems. Thus, the equilibrium points and corresponding stabilities in the system (6) are first analyzed. Letting $\dot{x}$=$\dot{y}$=$\dot{z}$=$\dot{\varphi}$=0, the equilibrium points can be solved by

$$\begin{cases} \alpha(z - x) + k_1 b x \varphi = 0 \\ \beta - z^2 = 0 \\ \gamma x y = 0 \\ c_1 x - d_1 h(\varphi) = 0 \end{cases} \tag{9}$$

Then the equilibrium equation (9) can be transformed as

$$\begin{cases} f_1(\varphi, x) = \alpha(\pm\sqrt{\beta} - x) + k_1 b x \varphi \\ f_2(\varphi, x) = c_1 x - d_1 h(\varphi) \end{cases} \tag{10}$$

Here, equation (10) is solved by using graphical analysis methods based on the MATLAB platform. Taking N=2 as an example, when b=0.1, c_1=2.6, d_1=2.4, k_1=-0.2, and initial states (0.1, 0.1, 0.1, 0.1), the distribution of the equilibrium points on the φ-x plane can be given by plotting the function curves f_1 colored in green and f_2 colored in red, as shown in Fig.5. As we can see, according to different positions, all equilibrium points are divided into two types E_1 and E_2. Then, the stability of these equilibrium points is analyzed by computing the Jacobin matrix and eigenvalues. Note that the Jacobin matrix of system (6) is the same at all equilibrium points. The results show that the same types of equilibrium points have the same eigenvalues. Also, all equilibrium points are nonhyperbolic equilibrium points. Hence, the stability of the original equilibrium points in the original system (5) is not changed. However, the number of the original equilibrium points is extended after introducing the memristor. Meanwhile, it can be found that the system (6) generates a connected 5-butterfly chaotic attractor in this case. To better observe the phenomenon, the phase trajectory of the 5-butterfly chaotic attractor is added to the equilibria distribution diagram,

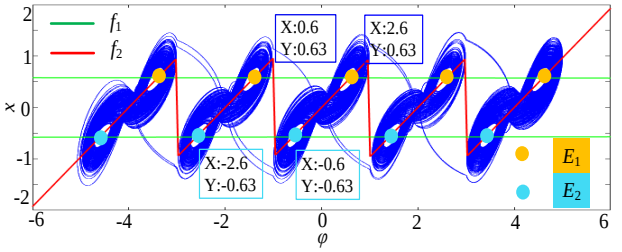

Figure 5: Equilibrium point distribution and corresponding phase trajectory of 1D-MMBCS with N=2 on the φ-x plane.

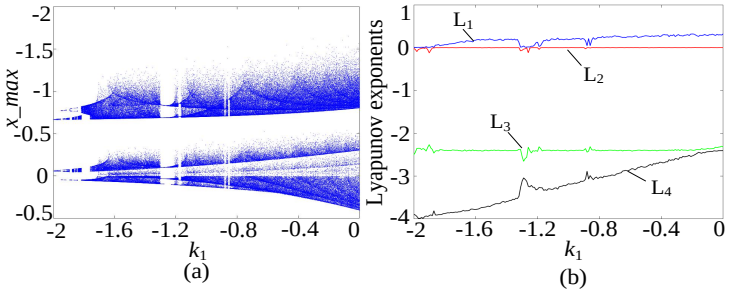

Figure 6: Chaotic dynamics of the 1D-MMBCS. (a) Bifurcation diagram. (b) Lyapunov exponents.

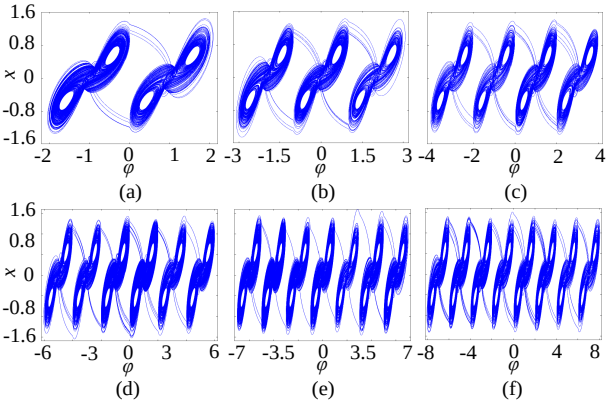

Figure 7: Connected 1D-MBCAs. (a) 2-butterfly attractor (M=0). (b) 3-butterfly attractor (N=1). (c) 4-butterfly attractor (M=1). (d) 6-butterfly attractor (M=2). (e) 7-butterfly attractor (N=3). (f) 8-butterfly attractor (M=3).

as shown in Fig.5. Clearly, each pair of equilibrium points (E_1 and E_2) correspond to a butterfly attractor. That is to say, the phase space of system (6) is extended to five parts along the φ-axis, in which each part represents an independent butterfly attractor. Keeping the above parameters unchanged, the bifurcation diagram and corresponding Lyapunov exponents of the 1D-MMBCS with respect to the parameter $k_1 \in (-2, 0)$ are plotted as shown in Fig.6. From Fig.6, the 1D-MMBCS presents multiple dynamical behaviors such as forward period-doubling bifurcation, period, and chaos. To further verify the above analysis, the different number of connected butterfly attractors are realized by setting different control parameters N and M, as shown in Fig.7. Further simulation shows that the equilibrium points can be extended regularly under the control of parameters N/M. Results show that system (6) can generate connected $(2N+1)$-butterfly attractors (odd number) and $(2M+2)$-butterfly attractors (even number). Therefore, the 1D-MMBCS generates arbitrary number of connected 1D-MBCAs.

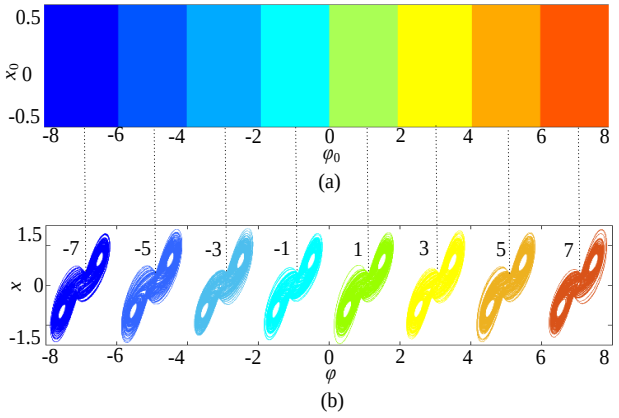

Figure 8: 1D-Initial-offset behavior of the 1D-MMBCS. (a) Basin of attraction related to φ_0. (b) Unconnected coexisting 8 butterfly attractors.

Initial-offset behavior is a special dynamical phenomenon that has infinitely many coexisting attractors with the same topology structure but different positions [49, 50]. Due to its special properties of extreme multistability, easy adjustability, and high flexibility, the Initial-offset behavior has attracted much attention recently [16,46]. Interestingly, the 1D-MMBCS can exhibit complex 1D-Initial-offset behavior. For example, keeping the above parameter values unchanged except for c_1=2, M=3, and the initial values $\varphi_0 \in$[-8, 8] and $x \in$[-0.5, 0.5], the local basin of attraction on the φ_0-x_0 plane is plotted in Fig.8(a). As can be seen, the basin of attraction has eight different regions painted with different colors. Here each region stands for the attraction regions of chaotic attractors with different positions. That is to say, the 1D-MMBCS can generate a series of coexisting chaotic attractors with different positions under different values of φ_0. To further verify this characteristic, with φ_0=±7, ±5, ±3, and ±1, coexisting eight butterfly attractors with the same topology structure are generated along the φ-axis, as shown in Fig.8(b). That is to say, the 1D-MMBCS generates unconnected multibutterfly chaotic attractors. Numerous simulations show that infinitely many unconnected butterfly attractors can be obtained with $N/M \to \infty$. Therefore, the 1D-MMBCS exhibits significant 1D-initial-offset behavior. This property is very significant in engineering applications because it can provide a mass of nondestructive and robust chaotic signals with different offset amplitudes.

3.2 Dynamical analysis of 2D-MMBCS

This subsection analyzes the equilibrium points, 2D-MBCAs, and 2D-initial-offset behavior of the 2D-MMBCS in the system (7). Letting $\dot{x}$=$\dot{y}$=$\dot{z}$=$\dot{\varphi}_1$=$\dot{\varphi}_2$=0, the equilibrium points can be solved by

$$\begin{cases} x = \left(d_1/c_1\right) h_1(\varphi_1) \\ y = 0 \\ z = \pm\sqrt{\beta} \\ f_1(\varphi_1, \varphi_2) = \alpha(z - x) + k_1 bx\varphi_1 = 0 \\ f_2(\varphi_1, \varphi_2) = h_2(\varphi_2) = 0 \end{cases} \tag{11}$$

Taking N_1=N_2=1 as an example, and setting b=0.1, c_1=2.6, d_1=2.4, c_2=3.5, d_2=2.5, k_1=-0.2, and k_2=-0.1, the distribution of equilibrium points on the φ_1-φ_2 plane is shown in Fig.9 where the function curve f_1 is colored in red and f_2 colored in green. It can be seen from Fig.9 that system (7) has two types of equilibrium points E_1 and E_2. That is to say, the two types of equilibrium points in the system (7) are extended along φ_1- and φ_2-directions, respectively. It also can be found that all equilibrium points are nonhyperbolic. Meanwhile, the system (7) generates a connected 3×3-butterfly chaotic attractor under this case with initial states (0.1, 0.1, 0.1, 0.1, 0.1). Its phase trajectory is covered in Fig.9 to better understander this dynamical phenomenon. Obviously, the phase space of system (7) is extended to 3×3 parts in the φ_1-φ_2 plane, in which each part represents an independent butterfly attractor. To further verify this characteristic, some typical connected 2D-MBCAs are given in Fig.10 with different control parameters. Evidently, as the control parameters N_i/M_i (i=1, 2) increase, connected $((2N_1 + 1)$ or $(2M_1 + 2)) \times ((2N_2 + 1)$ or $(2M_2 + 2))$-

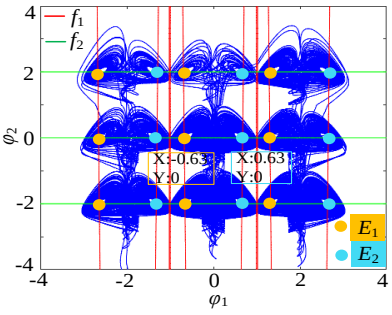

Figure 9: Equilibrium points distribution and corresponding phase trajectory of 2D-MMBCS with N_1=N_2=1 on the φ_1-φ_2 plane.

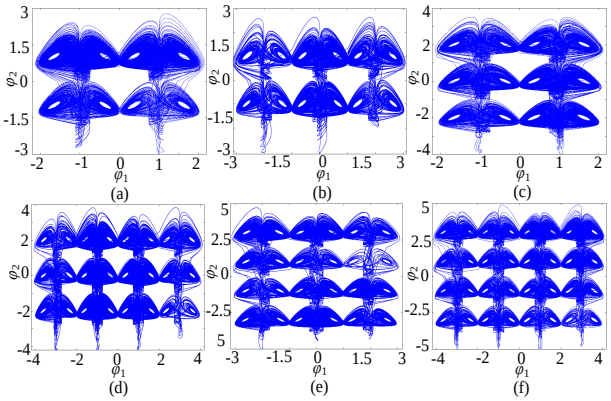

Figure 10: Connected 2D-MBCAs. (a) 2×2-butterfly attractor (M_1=0, M_2=0). (b) 3×2-butterfly attractor (N_1=1, M_2=0). (c) 2×3-butterfly attractor (M_1=0, N_2=1). (d) 4×3-butterfly attractor (M_1=1, N_2=1). (e) 3×4-butterfly attractor (N_1=1, M_2=1). (f) 4×4-butterfly attractor (M_1=1, M_2=1).

MBCAs can be obtained in the φ_1-φ_2 plane. Therefore, the 2D-MMBCS can generate arbitrary number of connected 2D-MBCAs.

Similarly, the constructed 2D-MMBCS can exhibit 2D-initial-offset behavior. To verify this property, we plot the local basin of attraction for the above parameters unchanged except for c_1=2, c_2=1, and N_1=N_2=1 in the φ_{10}-φ_{20} plane and show the results in Fig.11(a). It can be seen that the basin of attraction has nine different regions painted with different colors. Clearly, the Initial-offset behavior occurs along φ_1 and φ_2 directions, simultaneously, which shows the 2D-initial-offset behavior. Thus, the 2D-MMBCS can produce a series of unconnected coexisting chaotic attractors with different positions in the φ_1-φ_2 plane. Taking (φ_{10}, φ_{20})=(-2/0/2, -2/0/2) as an example, unconnected coexisting nine butterfly attractors can be obtained in the φ_1-φ_2 plane, as shown in Fig.11(b). Numerous simulations show that infinitely many unconnected coexisting butterfly attractors can be obtained with $N_i/M_i \to \infty$. Therefore, the constructed 2D-MMBCS has complex 2D-Initial-offset behavior. In other words, the 2D-MMBCS generates unconnected 2D-MBCAs. This means that it can provide nondestructive and robust chaotic signals with different offset amplitudes along two different directions.

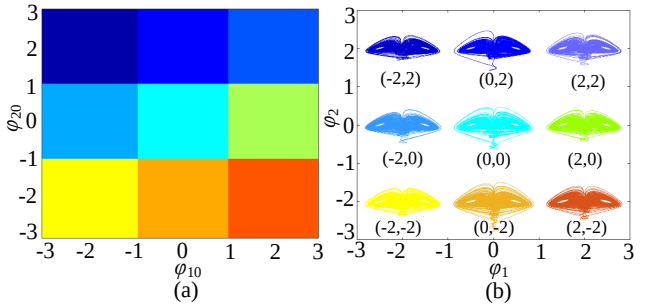

Figure 11: 2D-Initial-offset behavior of 2D-MMBCS. (a) Basin of attraction related to φ_{10} and φ_{20} values. (b) Unconnected coexisting 3×3 butterfly attractors.

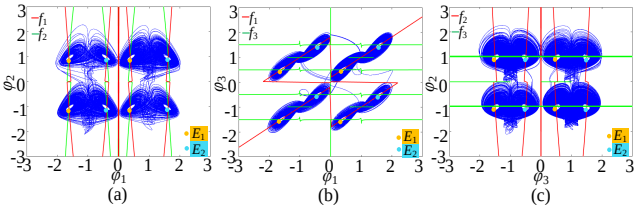

Figure 12: Equilibrium points distribution and corresponding phase trajectory of 3D-MMBCS with M_1=M_2=M_3=0. (a) φ_1-φ_2 plane. (b) φ_1-φ_3 plane. (c) φ_3-φ_2 plane.

3.3 Dynamical analysis of 3D-MMBCS

This subsection analyzes the equilibrium points, 3D-MBCAs, and 3D-initial-offset behavior of the 3D-MMBCS in the system (8). Letting $\dot{x}$=$\dot{y}$=$\dot{z}$=$\dot{\varphi}_1$=$\dot{\varphi}_2$=$\dot{\varphi}_3$=0, the equilibrium points can be solved by

$$\begin{cases} x = \left(d_1/c_1\right) h(\varphi_1) \\ y = \left(d_2/c_2\right) h(\varphi_2) \\ z = \left(d_3/c_3\right) h(\varphi_3) \\ f_1\left(\varphi_1, \varphi_3\right) = \alpha(z-x) + k_1 bx\varphi_1 = 0 \\ f_2\left(\varphi_2, \varphi_3\right) = \beta - z^2 + k_2 by\varphi_2 = 0 \\ f_3\left(\varphi_1, \varphi_2, \varphi_3\right) = \gamma xy + k_3 bz\varphi_3 = 0 \end{cases} \tag{12}$$

Keeping b=0.1, c_1=2.6, d_1=2.4, c_2=3.5, d_2=2.5, k_1=-0.2, and k_2=-0.1 unchanged, setting c_3=1.6, d_3=1.7, and k_3=0.2, and taking M_1=M_2=M_3=0 as an example, the distribution of equilibrium points on φ_1-φ_2, φ_1-φ_3, and φ_3-φ_2 planes is given in Fig.12(a), (b), and (c), respectively. It can be easily observed that equilibrium points of φ_1-, φ_2-, and φ_3-directions are extended, synchronously. Meanwhile, the corresponding phase spaces are also extended in the φ_1-φ_2 plane, φ_1-φ_3 plane, and φ_3-φ_2 plane, as shown in Fig.12(a), (b), and (c), respectively. So the number of butterfly attractors is 2×2×2. The corresponding connected 2×2×2-butterfly attractor is given in Fig.13(a). Evidently, as the control parameters N_i/M_i (i=1, 2, 3) increase, the butterfly attractor is extended in the φ_1-φ_2-φ_3 space. To further verify the above analysis, different number of connected 3D-MBCAs are realized by setting different control parameters, as shown in Fig.13. Clearly arbitrary number ($(2N_1+1)$ or $(2M_1+2)$)×($(2N_2+1)$ or $(2M_2+2)$)×($(2N_3+1)$ or $(2M_3+2)$) of connected 3D-MBCAs can be generated by 3D-MMBCS.

Surprisingly, the 3D-MMBCS can exhibit complicated 3D-Initial-offset behavior, which has not been reported in previous chaotic systems. For example, when keeping the above parameters unchanged except for c_1=2, c_2=1, c_3=1, M_1=M_2=M_3=3, the bifurcation diagrams with φ_{10} ∈[-8,8], φ_{20} ∈[-8,8], and φ_{30} ∈[-8,8] and corresponding first three Lyapunov exponents are plotted in Fig.14. As we can see, Fig.13(a_1), (a_2), and (a_3) show typical Initial-offset bifurcation phenomena with stair-stepping diagram. That is, the 3D-MMBCS simultaneously generates Initial-offset behavior along φ_{10}-, φ_{20}-, and φ_{30}-directions, respectively, which means that the 3D-Initial-offset behavior occurs. For further verifying this feature, setting eight sets of different initial states (φ_{10}, φ_{20}, φ_{30})=(-1/1, -1/1, -1/1), the phase portraits of unconnected coexisting 2×2×2 butterfly attractors can be produced in φ_1-φ_2-φ_3 space, as shown

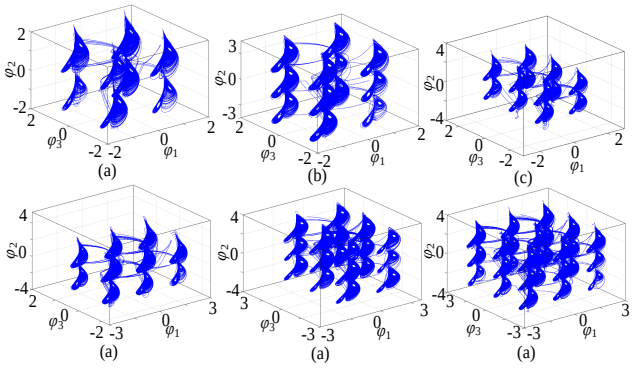

Figure 13: Connected 3D-MBCAs. (a) 2×2×2-butterfly attractor (M_1=M_2=M_3=0). (b) 2×3×2-butterfly attractor (M_1=M_3=0, N_2=1). (c) 2×2×3-butterfly attractor (M_1=M_2=0, N_3=1). (d) 3×2×2-butterfly attractor (N_1=1, M_2=M_3=0). (e) 2×3×3-butterfly attractor (M_1=0, N_2=N_3=1). (f) 3×3×3-butterfly attractor (N_1=N_2=N_3=1).

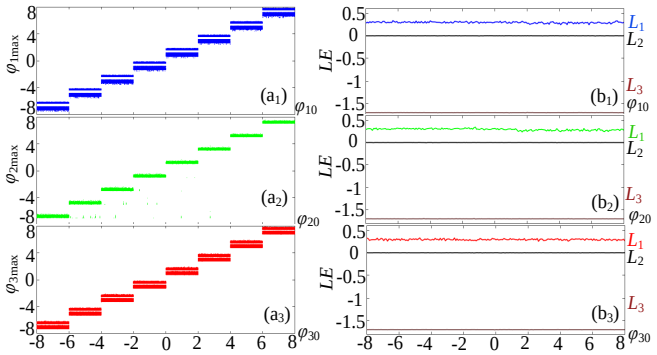

Figure 14: 3D-Initial-offset behavior of 3D-MMBCS. (a_1)-(a_3) Bifurcation diagram related to φ_{10}, φ_{20}, and φ_{30}, respectively. (b_1)-(b_3) Corresponding Lyapunov exponents.

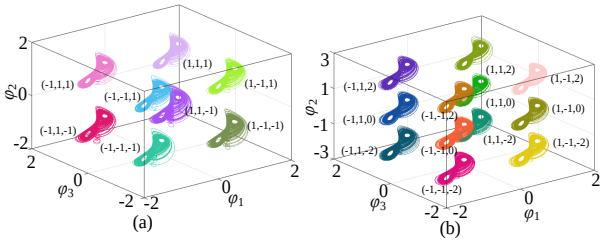

Figure 15: Unconnected coexisting butterfly attractors in φ_1-φ_3-φ_2 space. (a) Coexisting 2×2×2 butterfly attractors. (b) Coexisting 2×3×2 butterfly attractors.

in Fig.15(a). Furthermore, setting initial states (φ_{10}, φ_{20}, φ_{30})=(-1/1, -2/0/2, -1/1), unconnected coexisting 2×3×2 butterfly attractors can be obtained as shown in Fig.15(b).Obviously, the position of the unconnected multibutterfly attractors can be determined by switching memristors' initial states. That is, the 3D-MMBCS exhibits 3D-Initial-offset behavior. Thus the 3D-MMBCS can generate arbitrary number and position of the unconnected 3D-MBCAs, which shows that it can meet various signal requirements in practical applications.

To understand the obtained results of this section more quickly, the differences between the three MBCSs are summarized shortly. From a system structure point of view, the *m*D-MMBCS (*m*=1, 2, 3) with *m* coupling memristors is an (*m*+3)-dimensional dynamical system. From the equilibrium point distribution point of view, the 1D-, 2D-, and 3D-MMBCSs have a line equilibrium set, a plane equilibrium set, and a space equilibrium set, respectively. From

Table 1
Comparison of the MMBCSs with other MBCSs.

Properties	2016 [33]	2018 [34]	2019 [35]	2021 [36]	2021 [47]	This paper
Realization method	Piecewise-linear function	Stair switching function	Multilevel-logic pulse	Sinusoidal function	Multi-piecewise Memristor	Simplified multi-piecewise memristor
Extensibility in any direction	No	No	Yes	No	No	Yes
Attractor dimension	1D	2D	3D	1D	1D	3D
Controlable attractor position	No	No	No	No	No	Yes
Control parameters	non-integer	non-integer	non-integer	non-integer	Integer	Integer
Initial-offset behavior	No	No	No	No	1D	3D

a dynamics point of view, the mD-MMBCS can generate connected mD-MBCAs, mD-Initial-offset behavior, and unconnected coexisting mD-MBCAs.

4. Comparison analysis and circuit verification

This section mainly compares the existing MBCSs, and further proves the theoretical analysis and simulation results by designing analog circuits.

4.1 Comparison analysis

A comparison with existing MBCSs is given in Table 1. The evaluations are made from six aspects: Realization method, extensibility in any direction, attractor dimension, controllable attractor position, control parameters, and Initial-offset behavior. From an implementation perspective, the MBCSs in [33,34,36] were realized by using nonlinear switching functions, and the MBCS in [35] was designed by using a nonlinear switching pulse. These nonlinear switching methods exist some drawbacks in extensibility, controllability, dynamics, and circuit implementation, which makes them very inconvenient to adjust the number and position of butterfly attractors. Different from these nonlinear switching methods, this paper adopted simplified multi-piecewise memristors to construct a family of MBCS. Compared with the nonlinear switching methods, the memristor method has controllable attractor positions, simple integer parameters, and complex Initial-offset behaviors. Although Ref. [47] proposed an MBCS by using a multi-piecewise memristor, it only can generate 1D-multibutterfly chaotic attractors and 1D-Initial-offset behavior. On the contrary, the proposed method in this paper can be applied in any direction to construct 1D-, 2D-, and 3D-MBCSs. The constructed MMBCSs can generate 1D-, 2D-, and 3D-MBCAs. The number and position of butterfly attractors can be conveniently adjusted by changing integer control parameters and initial states. Especially, the proposed MMBCSs exhibit 1D-, 2D-, and 3D-Initial-offset behaviors, which have never been reported in previous work.

4.2 Circuit verification

The verification of chaotic systems with hardware circuits is of great theoretical and practical importance. Compared with digital circuit implementation [27], analog circuit implementation [51] has many advantages including low cost, high precision, and proven technique in the design of chaotic systems. In this section, a simple module-based analog circuit has been designed to implement the three MMBCSs discussed above.

According to the systems (6), (7), and (8), the circuit of the MMBCSs is designed as shown in Fig.16, where Mem1, Mem2, and Mem3 are simplified multi-piecewise memristor circuits given in Fig.2. It should be noted that three selecting switches T_1, T_2 and T_3 are added to the circuit to control different MMBCSs, as shown in Table 2. In other words, 1D-, 2D-, and 3D-MMBCSs can be realized from the same circuit in Fig.16 without changing the circuit structure. When T_1, T_2, and T_3 are closed, the circuit of the 3D-MBCS in the system (8) can be implemented.

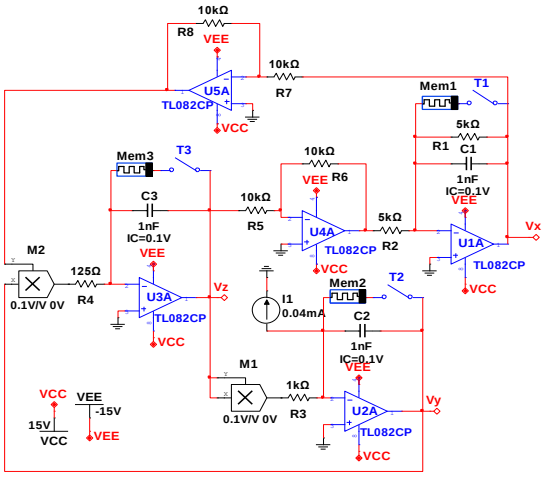

Figure 16: Circuit implementation of the MMBCSs.

Table 2
Switches and circuit parameters

Parameters	1D-MMBCS	2D-MMBCS	3D-MMBCS
T_1	On	On	On
T_2	Off	On	On
T_3	Off	Off	On
$R_{b1}/R_{c1}/R_{d1}$(kΩ)	50/3.84/4	50/3.84/4	50/3.84/4
$R_{b2}/R_{c2}/R_{d2}$(kΩ)	–	100/2.85/4	100/2.85/4
$R_{b3}/R_{c3}/R_{d3}$(kΩ)	–	–	166/6.25/5.88

According to Kirchhoff's circuit law, the circuit state equation is expressed as

$$\begin{cases} RC\dot{v}_x = \frac{R}{R_2}v_z - \frac{R}{R_1}v_x - \frac{Rgv_xv_{\varphi 1}}{R_{b1}} \\ RC\dot{v}_y = I_1 - \frac{gR}{R_3}v_z{}^2 - \frac{Rgv_yv_{\varphi 2}}{R_{b2}} \\ RC\dot{v}_z = \frac{gR}{R_4}v_xv_y + \frac{Rgv_zv_{\varphi 3}}{R_{b3}} \\ RC\dot{v}_{\varphi 1} = \frac{R}{R_{c1}}v_x - \frac{R}{R_{d1}}h_1(v_{\varphi 1}) \\ RC\dot{v}_{\varphi 2} = \frac{R}{R_{c2}}v_y - \frac{R}{R_{d2}}h_2(v_{\varphi 2}) \\ RC\dot{v}_{\varphi 3} = \frac{R}{R_{c3}}v_z - \frac{R}{R_{d3}}h_3(v_{\varphi 3}) \end{cases} \tag{13}$$

where RC denotes the integral time constant. Capacitor voltages v_x, v_y, and v_z represent the state variables x, y, and z, respectively. $v_{\varphi 1}$, $v_{\varphi 2}$ and $v_{\varphi 3}$ denote three memristor state variables φ_1, φ_2 and φ_3, respectively. Let R=10 kΩ, C_1=C_2=C_3=C=1 nF, RC=10 us. According to the system parameters in system (8), some circuit parameters can be set to I_1=0.04 mA, R_1=R_2=R/α=5 kΩ, R_3=$gR/1$=1 kΩ, R_4=gR/γ=0.125 kΩ, and some memristor circuit parameters can be computed by R_{bi}=Rg/k_ib_i, R_{ci}=R/c_i, R_{di}=R/d_i.

Based on the designed circuit in Fig.16, an analog hardware circuit is physically realized by using operational amplifiers TL082CP, analog multipliers AD633JN and ±15 V power voltages. According to the above logic, the three MMBCSs can be implemented by selecting different control switches and circuit parameters, as shown in Table 1. For 1D-MMBCS, when closing S_1 and S_2 and setting e_1=2 in the circuit of Mem1, a connected 4-butterfly chaotic attractor can be generated from the circuit, as shown in Fig.17(a). When closing S_2 and S_3, setting e_1=1, e_2=3, a connected 5-butterfly attractor can be obtained as shown in Fig.17(b). For 2D-MMBCS, when closing S_2 and setting e_1=1 in the circuit of Mem1, and closing S_1 in the Mem2, a connected 3×2-butterfly attractor is generated as shown in Fig.17(c).

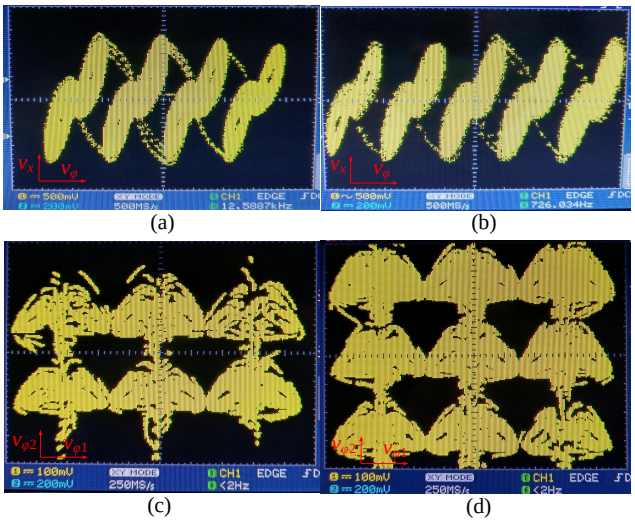

Figure 17: Experimental results of connected 1D- and 2D-MBCAs. (a) 4-butterfly attractor. (b) 5-butterfly attractor. (c) 3×2-butterfly attractor. (d) 3×3-butterfly attractor.

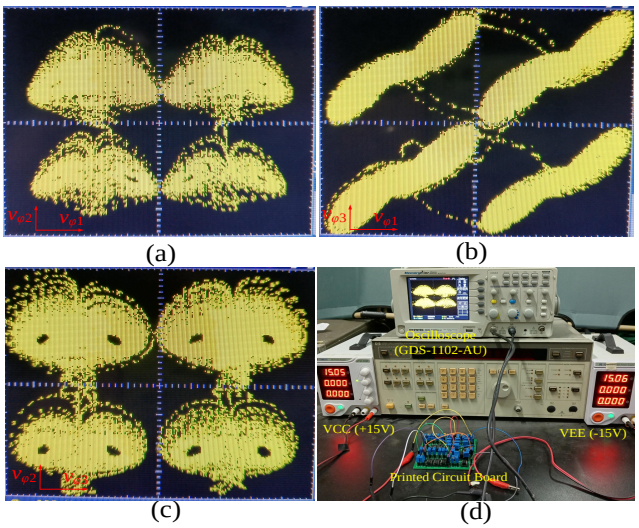

Figure 18: Experimental results of connected 2×2×2-butterfly attractor. (a) v_{φ_1}-v_{φ_2} plane. (b) v_{φ_1}-v_{φ_3} plane. (c) v_{φ_3}-v_{φ_2} plane. (d) Hardware experiment platform.

When only closing S_2 and setting e_1=1 in Mem1, and only closing S_2 and setting e_1=1 in Mem2, a connected 3×3-butterfly attractor can be realized as shown in Fig.17(d). For 3D-MMBCS, when synchronously closing S_1 in Mem1, Mem2, and Mem3, a connected 2×2×2-butterfly attractor can be observed by the oscilloscope as shown in Fig.18(a)-(c). It is clear that the number of butterflies can be systematically controlled by control voltages (e_i) and switches (S_i) in the memristor circuits. Besides, the experimental facility is shown in Fig.18(d). The size of printed circuit board is 9.2 cm× 9.2 cm.

In addition, because the initial states are hard to accurately set in analog circuits, various Initial-offset behaviors are verified by circuit simulation in the Multisim platform. Keeping the above parameters unchanged except for R_{c1}=$R/2$=5 kΩ, R_{c2}=$R/1$=10 kΩ, R_{c3}=$R/1$=10 kΩ, unconnected coexisting 1D-, 2D-, and 3D-MBCAs are generated from the circuit, as shown in Fig.19(a), (b) and (c_1-c_3), respectively. Clearly, experimental results agree with the numerical simulation results in Section II.

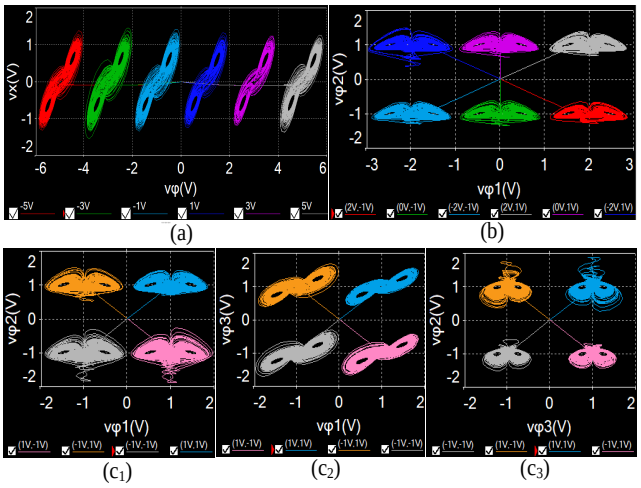

Figure 19: Experimental results of unconnected 1D-, 2D-, and 3D-MBCAs. (a) coexisting 6 butterfly attractors. (b) Coexisting 3×2 butterfly attractors. (c_1-c_3) Coexisting 2×2×2 butterfly attractors.

5. Application in telemedicine privacy protection

With the rapid development of information technology, telemedicine has become more and more popular [52]. However, privacy breaches of medical data have long been a pain point for the industry [53]. To solve this problem, here, we propose a new medical image encryption solution based on the designed MMBCSs.

5.1 Design of PNRG

Random number plays a key role in the application of digital data encryption [54,55]. Since the proposed MMBCSs can generate chaotic sequences with complex chaotic behaviors, they can achieve good performance in this application. We design pseudorandom number generators (PRNGs) using the chaotic sequences generated by 8-btterfly attrctor in 1D-MMBCS, 3×3-butterfly attractor in 2D-MMBCS, and 2×2×3-butterfly attractor in 3D-MMBCS, respectively. Firstly, a chaotic sequence S=($s_1, s_2, \ldots, s_n, \ldots$) is generated by the MMBCSs. Then, each value s_n in S is transformed into a 32-bit stream according to the IEEE 754 standard. Finally, the 15th-30th bits from the bit stream are truncated as pseudorandom numbers. The designed PRNG can be described as

$$P_i = B(s_n)_{15:30} \tag{14}$$

where $B(.)$ is to transform a value into a 32-bit float number obeying the IEEE floating point standard, and P is the obtained random number sequence. Hence, 16 bits numbers are produced for each output of the chaotic sequence. The random numbers are expected to have high randomness. The NIST SP800-22 is used to test the random numbers [56]. It is a convinced and all-side test standard that contains 15 sub-tests. According to the setting and requirements, we set the significance level as 0.01, and the test binary sequences are of length 10^6 bits. Then a total number of 160 binary sequences are generated and tested.

In our experiments, the initial states for MMBCSs are set to 0.1, and 160 binary sequences with length 10^6 bits are generated using the presented PRNG. To obtain more neutral test results, the first 5 binary sequences are discarded and the remaining 155 binary sequences are used for testing. According to the illustration in [56], the past-rate and p-value$T$ greater than 0.9609 and 0.0001 are considered to pass related subtest. Table 3 lists the test results of the four sets of chaotic sequences under different conditions, respectively. As can be seen, the pass-rate and p-value$T$ produced by different subtests are all larger than 0.9609 and 0.0001, respectively. This means that the MMBCSs have complex chaotic behaviors and can produce random numbers with high randomness.

5.2 Medical image encrypting solution

The concept map of the medical data encrypting solution is given in Fig.20. As shown in Fig.20, when a patient needs to see different doctors, he needs to send medical images to each doctor on the internet. During the transmission

Table 3
Test results of random numbers produced by pring using the MMBCSs in NIST SP800-22

No.	Sub-tests	1D-MMBCS		2D-MMBCS		3D-MMBCS	
		p-value$T$	Pass-rate	p-value$T$	Pass-rate	p-value$T$	Pass-rate
01	Frequency	0.3622	0.9643	0.1883	0.9714	0.8699	0.9714
02	Block Frequency	0.0254	0.9625	0.0257	1.0000	0.0235	0.9632
03	Cum.Sums*(F)	0.1125	0.9638	0.0444	0.9643	0.4373	0.9643
	Cum.Sums*(R)	0.0386	0.9632	0.0909	0.9857	0.6222	0.9643
04	Runs	0.8585	0.9714	0.6964	0.9786	0.6074	0.9635
05	Longest Runs	0.1830	1.0000	0.6964	0.9929	0.2660	0.9857
06	Rank	0.0187	0.9614	0.0147	0.9786	0.0157	0.9786
07	FFT	0.1916	0.9929	0.0612	0.9929	0.9018	0.9786
08	Non-Ovla.Temp.*	0.3814	0.9857	0.5778	0.9928	0.6520	0.9857
09	Ovla.Temp.	0.8699	0.9929	0.7955	0.9786	0.2475	0.9929
10	Universal	0.4506	0.9786	0.6073	0.9783	0.8585	0.9786
11	Appr.Entropy	0.7819	0.9857	0.7955	0.9929	0.3987	0.9929
12	Ran.Exc.*	0.3169	0.9873	0.2757	0.9747	0.2274	0.9872
13	Ran.Exc.Var.*	0.3826	0.9747	0.5768	0.9873	0.5056	0.9872
14	Serial (1st)	0.5341	0.9786	0.2386	0.9857	0.3863	0.9856
	Serial (2nd)	0.1501	0.9857	0.6222	0.9929	0.0424	0.9786
15	Linear Complexity	0.1625	0.9929	0.9449	0.9857	0.4641	1.0000

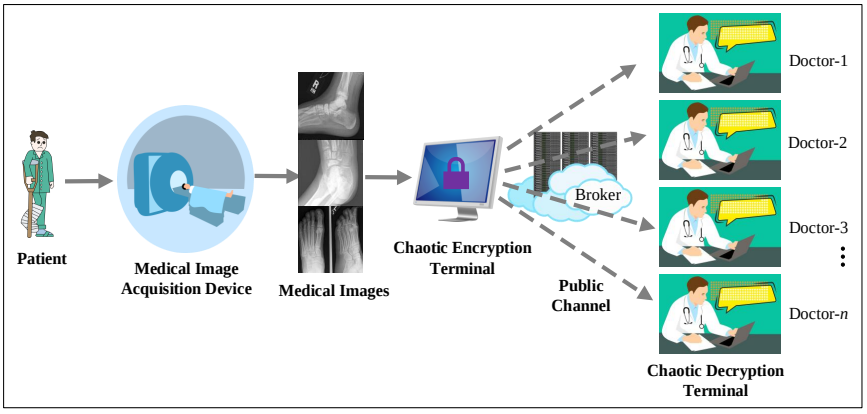

Figure 20: Concept map of medical data encrypting solution in online medical treatment.

of medical data, data that is not encrypted is vulnerable to theft. To better protect personal privacy, we encrypt medical data before it is sent. Decrypt the encrypted data when it is transmitted to the doctor through the common channel. As a result, medical data can be protected well. Next, a medical image encryption and decryption scheme are designed based on the PRNG generated from the proposed MMBCSs.

The encryption and decryption process is described in the following steps.

Step 1: Set α=2, β=0.4, γ=8, b=0.1, c_1=2.6, d_1=2.4, c_2=3.5, d_2=2.5, c_3=1.6, d_3=1.7, k_1=-0.2, k_2=-0.1, k_3=0.2, $N_1 = N_2 = N_3$=1, and initial states (0.1, 0.1, 0.1, 0.1, 0.1, 0.1), discarded number N=500, and time step Δt=0.001, the 3D-MMBCS is continuously iterated to generate $3 \times 3 \times 3$-butterfly sequences $x(i)$, $y(i)$, and $z(i)$.

Step 2: To obtain a pseudo-random sequence, the generated sequences are preprocessed as

$$\begin{cases} K_1(i) = (x(i) + y(i) + z(i))/3 \\ K_2(i) = \mathrm{mod}(\mathrm{floor}(((x(i) + y(i) + z(i))/3) * 10^{15}), 256) \end{cases} \tag{15}$$

where the floor(x) is the elements of x to the nearest integer less than or equal to x.

Step 3: The chaotic sequence $K_1(i)$ is arranged in ascending order to obtain the index sequence index.

Step 4: According to the index sequence index, the original image $P(i)$ is globally scrambled to be a sequence $P_1(i)$

$$P_1(i) = P(index(K_1(i))) \tag{16}$$

So, the pixel of the original image is permutated by using $K_1(i)$.
Step 5: The processed images $P_1(i)$ is encrypted by means of XOR operation, as follows

$$C(i) = P_1(i) \oplus K_2(i) \tag{17}$$

The chaotic system is iterated until all elements are encrypted.
Step 6: Finally, an encrypted image is obtained by converting each element in the encrypted set to a decimal number.
Step 7: Decryption is the reverse process of the encryption operation.

5.3 Performance analysis

To demonstrate the efficiency of the designed medical image encryption scheme, three CT medical images (Foot-1, Foot-2, Foot-3) with a size of 256×256 are chosen as the encryption object. The experimental results and security performance analysis including histogram, correlation coefficient, information entropy, key sensitivity, data loss, and noise attack are as follows. Noted that the fourth-order Runge-Kutta algorithm is utilized in the Matlab numerical simulation, where the start time and the time step are fixed as 500 and 0.001, respectively.

(1) Histogram analysis: The image's distribution of pixel intensity values is depicted using histograms. A uniform histogram should be produced by an effective image encryption system for the best results. The original images, encrypted image, and their respective histograms are depicted in Fig.21. The encrypted image in Fig.21(c1-c3) clearly appears cluttered and has lost all original information. Because the encrypted image's histogram in Fig.21(d1-d3) is almost uniform, it is difficult to extract any useful statistical information from it. Consequently, the proposed method for image encryption is sufficient to withstand statistical attacks.

(2) Correlation analysis: The relationship between adjacent pixels in the image is reflected in the correlation. In a typical image, there is typically a strong correlation in three directions between adjacent pixels. The correlation coefficient can be obtained by [35, 36]

$$\rho_{xy} = \frac{\sum_{i=1}^{N}(x_i - E(x))(y_i - E(y))}{\sqrt{\sum_{i=1}^{N}(x_i - E(x))^2}\sqrt{\sum_{i=1}^{N}(y_i - E(y))^2}} \tag{18}$$

where x and y represent the intensity values of two adjacent pixels. In this case, the correlation coefficient is computed by randomly selecting 10,000 pairs of horizontal, vertical, and diagonal pixels from the encrypted image and the original image. Table 4 displays the original and encrypted images' respective correlation coefficients. Table 4 demonstrates that the correlation coefficient of the original image is very close to the maximum value of 1, whereas the encrypted image's correlation coefficient is very close to the ideal value of zero. There is no doubt that the proposed method for encrypting images has the potential to significantly reduce the correlation between the original images. As a result, statistical attacks are greatly thwarted by the constructed medical image encryption scheme.

(3) Entropy analysis: The randomness of image information is reflected in information entropy. The information entropy is described by [36, 37]

$$H(P) = \sum_{i=0}^{2^N-1} P(x_i)\log_2\frac{1}{P(x_i)} \tag{19}$$

where $P(x_i)$ represents the probability of x_i and $2N$ is the number of the information source. Theoretically, the maximum information entropy value is 8. Information entropy calculation results for original and encrypted images are shown in Table 4. It can be seen from Table 4 that the information entropy of the encrypted images is very close to the ideal value. Compared with similar image encryption schemes based on different multibutterfly chaotic systems, the scheme proposed in this paper has higher information entropy.

(4) Sensitivity analysis: An important indicator of an encryption algorithm's security is its key sensitivity. Good image encryption schemes have a high key sensitivity. This encryption algorithm uses the initial values as secret

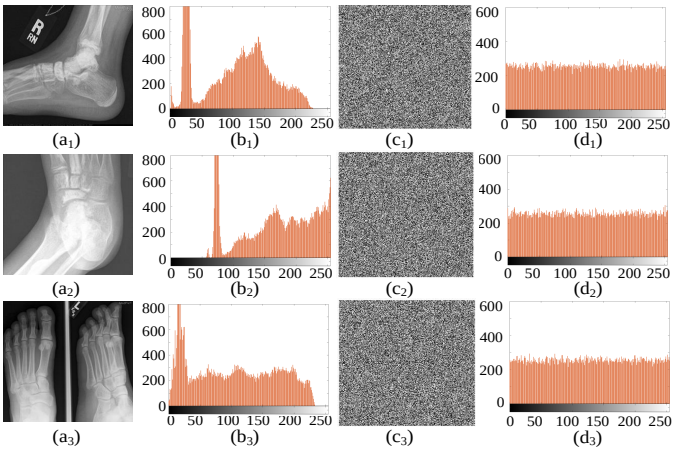

Figure 21: Encryption results: (a1)-(a3) original images (Foot-1, Foot-2, Foot-3). (b1)-(b3) histograms of the original images. (c1)-(c3) encrypted images. (d1)-(d3) histograms of the encrypted images.

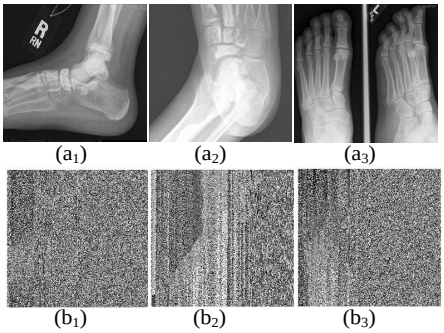

Figure 22: Sensitivity test results with the secret key (x_0, y_0, z_0). (a1)-(a3) Accurate decrypted images with the secret keys (0.1, 0.1, 0.1). (b1) Inaccurate decrypted image with an inaccurate secret key x_0=0.1+10^{-14}. (b2) Inaccurate decrypted image with an inaccurate secret key y_0=0.1+10^{-14}. (b3) Inaccurate decrypted image with an inaccurate secret key y_0=0.1+10^{-14}.

keys. Fig.22(a) depicts the decrypted image with the correct secret key. The incorrect decrypted image is depicted in Fig.22(b)-(d) with a minor modification to the secret key. The decrypted image is completely distinct from the original image, despite the slight modification to the secret key (10^{-14}). The proposed image encryption method has a higher sensitivity to the key than other similar methods, as shown in Table 4.

(5) Data loss and noise attacks: During transmission, image data is susceptible to loss of data and noise. Data loss and noise attacks should be prevented by an effective image encryption strategy. We cut off and decrypted a portion of the encrypted image to test the scheme's resistance to data loss. Data loss attacks for the various lost areas are successfully decrypted in Fig.23(a1)-(a4) for the original image to be recovered. The encrypted image is given salt and pepper noise of varying densities to test the algorithm's resistance to salt noise attacks. Despite the fact that some of the pixel values in the decrypted images have changed, the approximate information of the original image can still be successfully recovered, as shown in Fig.23(c1-c4) and Fig.23(d1-d4). We can conclude from the experimental results in Fig.23 that the proposed encryption algorithm is highly secure and resistant to data loss and noise attacks. In addition, the design scheme's and other encryption schemes' resistance to noise and data loss attacks (NADLA) were listed in Table 4. The findings demonstrate that the proposed scheme has superior encryption performance to other options.

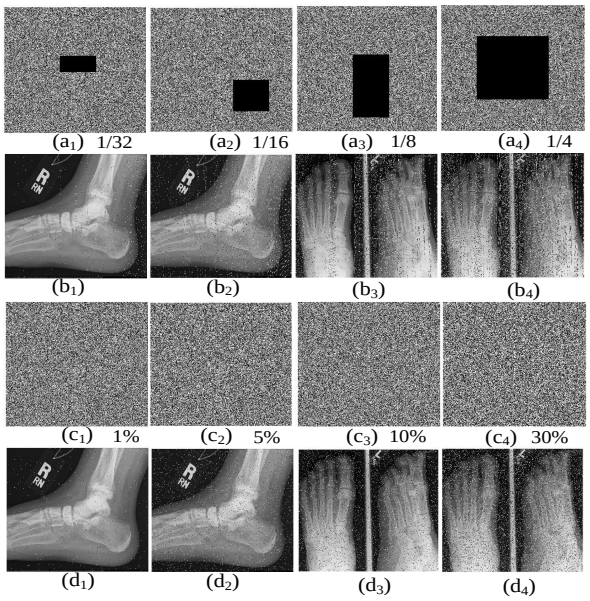

Figure 23: The test results of data loss and noise attacks. (a1)-(a4) the encrypted images with 1/32, 1/16, 1/8, and 1/4 loss, respectively. (b1)-(b4) corresponding decrypted images. (c1)-(c4) the encrypted images with 1%, 5%, 10%, and 30% salt and pepper noise, respectively. (d1)-(d4) corresponding decrypted images.

Table 4
Comparison of the test results.

Images	Horizontal original/encrypted	Vertical original/encrypted	Diagonal original/encrypted	Entropy original/encrypted	Key Sensitivity	Resisting NADLA
Lena [35]	– –	0.8952/0.004614	0.9583/0.01057	– –	10-12	No
Lena [36]	0.972807/0.000827	0.939337/0.005238	0.921438/0.000455	7.3740/7.9976	10-9	No
Lena [57]	0.94505/0.000682	0.96653/0.00077	0.91917/0.003636	7.3740/7.9974	– –	No
Foot-1	0.988139/0.003747	0.985131/0.004762	0.974845/0.000936	7.2116/7.9977	10-14	Yes
Foot-2	0.997963/0.010988	0.996757/0.005072	0.994470/0.003598	6.8134/7.9977	10-14	Yes
Foot-3	0.995264/0.008454	0.983932/0.008454	0.983797/0.001594	7.6845/7.9977	10-14	Yes

6. Conclusion

The memristor shows great merit to design chaotic systems with complicated dynamics. In this paper, different number of memristors are coupled into a modified Sprott C system and thus three memristive multibutterfly chaotic systems are constructed including 1D-, 2D-, and 3D-MMBCSs. Analysis results show that the three MMBCSs not only generate connected 1D-, 2D-, and 3D-MBCAs, respectively, but also produce unconnected 1D-, 2D-, and 3D-MBCAs, respectively. It is found that the memristors play key roles in the control of the number and position of connected and unconnected MBCAs. Moreover, the MMBCSs exhibit complex 1D-, 2D-, and 3D-Initial-offset behaviors, respectively. From the viewpoint of dynamics, the dynamical behaviors of the designed MMBCSs are more complex and abundant than the coexisting MBCSs. Analog circuit experiment demonstrates complex dynamics including connected and unconnected MBCAs. The medical data encryption scheme in telemedicine is further designed using different chaotic attractors to show the practical application of the MMBCSs. With the outstanding features, these proposed MMBCSs are expected to be used in many industry scenarios [58–60]. To the best of our knowledge, the phenomenon of the connected and unconnected multi-directional multiple chaotic attractors in the same chaotic system is rarely reported. Further study is still needed to explore its key theory and application in engineering.

Declaration of Competing Interest

The authors declare that they have no potential conflict of interest.

Acknowledgments

This work is supported by The National Natural Science Foundation of China (62201204, 62271197, 61971185), The China Postdoctoral Science Foundation (2022M71104), and The Natural Science Foundation of Hunan Province (2023JJ40168, 2022JJ30160, 2022JJ40514).

References

[1] Z. T. Njitacke, N. Tsafack, B. Ramakrishnan, et al, "Complex dynamics from heterogeneous coupling and electromagnetic effect on two neurons: Application in images encryption," *Chaos Solitons Fractals*., vol. 153, p. 111577, 2021.

[2] H. Li, Z. Hua, H. Bao, et al, "Two-dimensional memristive hyperchaotic maps and application in secure communication," *IEEE Trans. Ind. Electron*., vol. 68, no. 10, pp. 9931-9940, 2022.

[3] X. Ma, C. Wang, "Hyper-chaotic image encryption system based on N+ 2 ring Joseph algorithm and reversible cellular automata," *Multimed. Tools Appl*., vol. 1, pp. 1-26, 2023.

[4] E. N. Lorenz, "Deterministic nonperiodic flow," *J. Atmos. Sci*., vol. 20, no. 2, pp. 130-141, 1963.

[5] G. Cheng, R. Gui, "Bistable chaotic family and its chaotic mechanism," *Chaos Solitons Fractals*., vol. 162, p. 112407, 2022.

[6] D. Veeman, M. Mehrabbeik, H. Natiq, et al, "A new chaotic system with coexisting attractors," *Int. J. Bifurcation Chaos*., vol. 32 no. 3, p. 2230007, 2022.

[7] M. Ji'e, D. Yan, S. Sun, et al, "A simple method for constructing a family of Hamiltonian conservative chaotic systems," *IEEE Trans. Circuits Syst. I-Regul. Pap*., vol. 69, no. 8, pp. 3328-3338, 2022.

[8] Q. Lai, Z. Wan, P. D. K. Kuate, et al, "Coexisting attractors, circuit implementation and synchronization control of a new chaotic system evolved from the simplest memristor chaotic circuit," *Commun. Nonlinear Sci. Numer. Simul*., vol. 89, p. 105341, 2020.

[9] R. Wang, C. Li, S. Kong, et al, "A 3D memristive chaotic system with conditional symmetry," *Chaos Solitons Fractals*., vol. 158, p. 111992, 2022.

[10] H. Bao, Z. Chen, J. Cai, et al, "Memristive cyclic three-neuron-based neural network with chaos and global coexisting attractors," *Sci. China Technol Sc*., vol. 65, no.11, pp. 2582-2592, 2022.

[11] W. Zhou, G. Wang, H. H. C. Iu, et al, "Complex dynamics of a non-volatile memcapacitor-aided hyperchaotic oscillator," *Nonlinear Dyn*., vol. 100, no. 4, pp. 3937-3957, 2020.

[12] Q. Xu, X. Tan, Y. Zhang, et al, "Riddled attraction basin and multistability in three-element-based memristive circuit," *Complexity*., vol. 2020, p. 4624792, 2020.

[13] B. Mezatio, M. Motchongom, B. Tekam, et al, "A novel memristive 6D hyperchaotic autonomous system with hidden extreme multistability," *Chaos Solitons Fractals*., vol. 120, pp. 100-1115, 2019.

[14] Q. Lai, Z. Wan, L. K. Kengne, et al, "Two-memristor-based chaotic system with infinite coexisting attractors," *IEEE Trans. Circuits Syst. II-Express Briefs*., vol. 68, no. 6, pp. 2197-2201, 2020.

[15] S. Gu, S. He, H. Wang, et al, "Analysis of three types of initial offset-boosting behavior for a new fractional-order dynamical system," *Chaos Solitons Fractals*., vol. 143, p. 110613, 2021.

[16] H. Lin, C. Wang, F. Yu, et al, "A review of chaotic systems based on memristive hopfield neural networks," *Mathematics* ., vol. 11, no. 6, p. 1369, 2023.

[17] Q. Wan, F. Li, S. Chen, et al, "Symmetric multi-scroll attractors in magnetized Hopfield neural network under pulse controlled memristor and pulse current stimulation," *Chaos Solitons Fractals*., vol. 169, p. 113259, 2023.

[18] X. Zhang, C. Li, Y. Chen, et al, "A memristive chaotic oscillator with controllable amplitude and frequency," *Chaos Solitons Fractals*., vol. 139, p. 110000, 2020.

[19] F. Yuan, S. Li, Y. Deng, et al, "Cu-doped TiO2-x nanoscale memristive applications in chaotic circuit and true random number generator," *IEEE Trans. Ind. Electron*., vol. 70, no. 04, pp. 4120-4127, 2023.

[20] H. Lin, C. Wang, J. Sun, et al, "Memristor-coupled asymmetric neural networks: Bionic modeling, chaotic dynamics analysis and encryption application," *Chaos Solitons Fractals*., vol. 166, p. 112905, 2023.

[21] S. Ahmad, A. Ullah, A. Akgül, "Investigating the complex behaviour of multi-scroll chaotic system with Caputo fractal-fractional operator," *Chaos Solitons Fractals*., vol. 146, p. 110900, 2021.

[22] N. Wang, C. Li, H. Bao, et al, "Generating multi-scroll Chua's attractors via simplified piecewise-linear Chua's diode," *IEEE Trans. Circuits Syst. I-Regul. Pap*., vol. 66, no. 12, pp. 4767-4779, 2019.

[23] S. Sahoo, B. Roy, "Design of multi-wing chaotic systems with higher largest Lyapunov exponent," *Chaos Solitons Fractals*., vol. 157, p. 111926, 2022.

[24] H. Lin, C. Wang, Y. Sun, et al, "Generating-scroll chaotic attractors from a memristor-based magnetized Hopfield neural network," *IEEE Trans. Circuits Syst. II-Express Briefs*., vol. 70, no. 1, pp. 311-315, 2023.

[25] X. Liu, X. Tong, Z. Wang, et al, "Construction of controlled multi-scroll conservative chaotic system and its application in color image encryption," *Nonlinear Dyn*., vol. 110, no. 1, pp. 1897-1934, 2022.

[26] S. Sahoo, B. K. Roy, "Design of multi-wing chaotic systems with higher largest Lyapunov exponent," *Chaos Solitons Fractals*., vol. 157, p. 111926, 2022.

[27] Q. Lai, X. W. Zhao, K. Rajagopal, et al, "Dynamic analyses, FPGA implementation and engineering applications of multi-butterfly chaotic attractors generated from generalised Sprott C system," *Pramana*., vol. 90, no. 1, pp. 1-12, 2018.

[28] Q. Wu, Q. Hong, X. Liu, et al, "Constructing multi-butterfly attractors based on Sprott C system via non-autonomous approaches," *Chaos*., vol. 29, no. 4, p. 043112, 2019.

[29] Y. Huang, P. Zhang, W. Zhao, "Novel grid multiwing butterfly chaotic attractors and their circuit design," *IEEE Trans. Circuits Syst. II-Express Briefs*., vol. vol. 62, no. 5, pp. 496-500, 2015.

[30] F. R. Tahir, R. S. Ali, V. T. Pham, et al, "A novel 4D autonomous 2n-butterfly wing chaotic attractor," *Nonlinear Dyn*., vol. 85, no. 4, pp. 2665-2671, 2016.

[31] Q. Wu, Q. Hong, X. Liu, et al, "A novel amplitude control method for constructing nested hidden multi-butterfly and multiscroll chaotic attractors," *Chaos Solitons Fractals*., vol. 134, p. 109727, 2020.

[32] S. Yu, J. Lü, X. Yu, et al, "Design and implementation of grid multiwing hyperchaotic Lorenz system family via switching control and constructing super-heteroclinic loops," *IEEE Trans. Circuits Syst. I, Reg. Papers*., vol. 59, no. 5, pp. 1015-1028, 2012.

[33] Z. Wang, J. Ma, S. Cang, et al, "Simplified hyper-chaotic systems generating multi-wing non-equilibrium attractors," *Optik*., vol. 127, no. 5, pp. 2424-2431, 2016.

[34] N. Yu, Y. W. Wang, X. K. Liu, et al, "3D grid multi-wing chaotic attractors," *Int. J. Bifurcation Chaos*., vol. 28, no. 04, p. 1850045, 2018.

[35] Q. Hong, Y. Li, X. Wang, et al, "A versatile pulse control method to generate arbitrary multidirection multibutterfly chaotic attractors," *IEEE Trans. Comput-Aided Des. Integr. Circuits Syst*., vol. 38, no. 8, pp. 1480-1492, 2019.

[36] H. Lin, C. Wang, F. Yu, et al, "An extremely simple multiwing chaotic systempp. dynamics analysis, encryption application, and hardware implementation," *IEEE Trans. Ind. Electron*., vol. 68, no. 12, pp. 12708-12719, 2021.

[37] D. B. Strukov, G. S. Snider, D. R. Stewart, et al, "The missing memristor found," *Nature*., vol. 453, no. 7191, pp. 80-83, 2008.

[38] X. Ma, J. Mou, L. Xiong, et al, "A novel chaotic circuit with coexistence of multiple attractors and state transition based on two memristors," *Chaos Solitons Fractals*., vol. 152, p. 111363, 2021.

[39] Z. Li, H. Zhou, M. Wang, et al, "Coexisting firing patterns and phase synchronization in locally active memristor coupled neurons with HR and FN models," *Nonlinear Dyn*., vol. 104, pp. 1455-1473, 2021.

[40] H. Lin, C. Wang, L. Cui, et al, "Hyperchaotic memristive ring neural network and application in medical image encryption," *Nonlinear Dyn*., vol. 110, no. 1, pp. 841-855, 2022.

[41] Z. Guo, Z. Li, M. Wang, et al, "Hopf bifurcation and phase synchronization in memristor-coupled Hindmarsh-Rose and FitzHugh-Nagumo neurons with two time delays," *Chinese Physics B*., vol. 32, no. 3, pp. 38701-038701, 2023.

[42] M. Chen, M. Sun, H. Bao, et al, "Flux–charge analysis of two-memristor-based Chua's circuit: dimensionality decreasing model for detecting extreme multistability," *IEEE Trans. Ind. Electron*., vol. 67, no. 3, pp. 2197-2206, 2020.

[43] Y. Jiang, C. Li, C. Zhang, et al, "A double-memristor hyperchaotic oscillator with complete amplitude control," *IEEE Trans. Circuits Syst. I, Reg. Papers*., vol. 68, no. 12, pp. 4935-4944, 2021.

[44] B. Bao, K. Rong, H. Li, et al, "Memristor-coupled logistic hyperchaotic map," *IEEE Trans. Circuits Syst. II-Express Briefs*., vol. 68, no. 8, pp. 2992-2996, 2021.

[45] L. Zhou, C. Wang, L. Zhou, "A novel no-equilibrium hyperchaotic multi-wing system via introducing memristor," *Int. J. Circuit Theory Appl*., vol. 46, no. 1, pp. 84-98, 2018.

[46] S. Zhang, C. Li, J. Zheng, et al, "Generating any number of initial offset-boosted coexisting chua's double-scroll attractors via piecewise-nonlinear memristor," *IEEE Trans. Ind. Electron*., vol. 69, no. 7, pp. 7202-7212, 2021.

[47] S. Zhang, C. Li, J. Zheng, et al, "Generating any number of diversified hidden attractors via memristor coupling," *IEEE Trans. Circuits Syst. I-Regul. Pap*., vol. 68, no. 12, pp. 4945-4956, 2021.

[48] J. C. Sprott, "Some simple chaotic flows," *Phys. Rev. E*., vol. 50, no. 2, p. R647, 1994.

[49] X. Leng, B. Tian, L. Zhang, et al, "Study of a novel conservative chaotic system with special initial offset boosting behaviors," *Chaos*., vol. 32, no. 7, p. 073102, 2022.

[50] H. Wu, J. Zhou, M. Chen, et al, "DC-offset induced asymmetry in memristive diode-bridge-based Shinriki oscillator," *Chaos Solitons Fractals*., vol. 154, p. 111624, 2022.

[51] Y. Liang, G. Wang, G. Chen, et al, "S-type locally active memristor-based periodic and chaotic oscillators," *IEEE Trans. Circuits Syst. I, Reg. Papers*., vol. 67, no. 12, pp. 5139-5152, 2020.

[52] H. Estiri, Z. Strasser, J. Klann, et al, "Predicting COVID-19 mortality with electronic medical records," *NPJ digital medicine*., vol. 4, no. 1, pp. 15, 2021.

[53] Ghubaish, A., Salman, T., Zolanvari, M., et al, "Recent advances in the internet-of-medical-things (IoMT) systems security," *IEEE Internet of Things Journal*., vol. 8, no. 11, pp. 8707-8718, 2020.

[54] Z. Yang, Y. Liu, Y. Wu, et al, "A high speed pseudo-random bit generator driven by 2D-discrete hyperchaos," *Chaos Solitons Fractals*., vol. 167, p. 113039, 2023.

[55] Y. Zhu, C. Wang, J. Sun, et al, "A chaotic image encryption method based on the artificial fish swarms algorithm and the DNA coding," *Mathematics*., vol. 11, pp. 767. 2023.

[56] A. Rukhin, J. Soto, and J. Nechvatal, A statistical test suite for random and pseudorandom number generators for cryptographic applications, National Institute of Standards and Technology (NIST), Special Publication 800-22, Rev. 1a, Apr. 2010.

[57] F. Yu, L. Liu, S. Qian, et al, "Chaos-based application of a novel multistable 5D memristive hyperchaotic system with coexisting multiple attractors," *Complexity*., vol. 2020, Art. no. 8034196, 2020.

[58] X. Ma, C. Wang, Q. Wan, et al, "A fast hyperchaotic image encryption scheme," *Int J Bifur Chaos*., vol. 33, Art. no. 2350061, 2023.

[59] F. Kenmogne, S. Noubissie, G. Ndombou, et al, "Dynamics of two models of driven extended jerk oscillators: Chaotic pulse generations and application in engineering," *Chaos Solitons Fractals*., vol. 152, p. 111291, 2021.

[60] S. Xu, X. Wang, X. Ye, "A new fractional-order chaos system of Hopfield neural network and its application in image encryption," *Chaos Solitons Fractals*., vol. 157, p. 111889, 2022.